SIR-C / X-SAR Observations of Rain Storms

A.R. Jameson ‘,
F.K. Li [2],
S.L. Durden 2
Z.S. Haddad [2],
B. Holt [2],
‘T. Fogarty [2],
and
R.K. Moore ‘i.

January 4, 1996

Corresponding Author: Z.S. Haddad, 300- 227, Jet Propulsion Laboratory, 4800 Oak Grove Drive, Pasadena CA 91109-O8W

[1] RJH Scientific, Alexandria, VA
[2] Jet Propulsion Laboratory, California Institute of Technology, Pasadena CA
[3] University of Kansas, Lawrence KS

Abstract

The SIR-C / X-SAR radar observations of rain storms are the first multi-polarization and multi-frequency observations of precipitation from space. In addition to numerous often dramatic images of severe weather systems obtained by forming a synthetic aperture in the usual side-looking attitude, several data takes were performed while the radar antennas were parallel to the ground and the radar beams were pointing at nadir. These opportunities coincided with the passage of the Shuttle over Tropical Cyclone Odille in the southern Indian Ocean during the first flight, and over Typhoon Seth in the Western Pacific during the second flight. The resulting observations, or, more appropriately, the resulting *measurements*, demonstrate for the first time the capability of a spaceborne multi-frequency multi-polarization microwave radar system to quantify precipitation rates, to detect hydrometeor phase, and to classify rain type.

1 Introduction

While ground-based radars fulfill a critical role in monitoring severe weather systems that pass within their vicinity, the main advantage of a space-borne radar is that it provides global coverage. Another advantage is that, thanks to its "look-down" geometry, a space-borne radar can measure quite accurately the reflectivity of the hydrometeors within a storm as a function of altitude. Such measurements can help determine the nature and the amount of hydrometeors. Since there are many unknown physical parameters to be estimated in this problem (including the size distribution of the hydrometeors, and their geometric distribution within the radar beam), a single radar channel can scarcely be sufficient to quantify the 3-dimensional structure of the precipitation with much accuracy.

This paper describes the Shuttle Radar Laboratory (SRL) SIR-C / X-SAR radar observations of rainstorms, the first multi-polarization and multi-frequency measurements of precipitation from space. The main goals of the rain experiment were to verify the potential for the estimation of rainfall using two microwave radar frequencies, to demonstrate that polarization does enhance the ability to detect the freezing layer (the radar "bright band"), and to determine the effect of rainfall on the ocean surface backscatter.

Data were collected from two geometric attitudes: side-looking and nadir. The side-looking observations were taken and have been processed by forming a synthetic aperture. The resulting images are described in section 3. On the other hand, the nadir observations were obtained by having the Shuttle roll so that the radar antennas were parallel to the ground. The radars were then acting as profiling scatterometers, and the resulting measurements were therefore more readily amenable to quantitative interpretation. These nadir observations are described in section 2.

2 Nadir Observations

When operating in a side-looking mode, the vertical dimensions of the radar beams essentially integrate over the entire depth of the troposphere. Since the change in atmospheric parameters is generally greatest in the vertical, the large extent of the beams in that direction in effect obscures much of this important atmospheric stratification. Therefore, in order to improve the vertical resolution, the Shuttle was rolled on a few occasions so that the beams pointed directly at the surface of the Earth. The challenge of this procedure, however, was the timing of the roll so that there would likely be precipitation in the beams sometime during the brief period of data collection. By developing decision rationales and procedures over the last few years and, quite frankly, because of good luck, we managed to collect some interesting observations at nadir in precipitation. Before considering these

measurements, however, it is important to mention that precipitating systems [all int o two general categories, namely "convective systems" extending vertically over a significant fraction of the depth of the troposphere and "str atified syster ns" of weak convection (small vertical air motion) in which the precipitation evolution is largely confined to layers largely in the lower troposphere. The former are associated with more intense precipitation, and, consequently, greater backscattered signals over several kilometers, while the latter are usually characterized by **weak** signals with the strongest backscatter occurring near the melting level. (Consequently, depending upon several factors such as the radar sensitivity and distance to the targets, **it,** is feasible to use SIR-C / X-SAR measurements to compute vertical profiles of precipitation in convective systems, but n o t in stratiform ones.

Nadir measurements were obtained during one data take (1) T 34 .55) on SRL- 1, and during three data takes (DT's **45.5 , 54.0** and 103.0) 011 SRL-2. During these dat a takes, measurements were collected with VV and VH polarizations at C- and L-b ar ids, and with VV polarization at X-band. The short pulse length (8.44 /me) **and** the narrow bandwidth (1 0MHz) were selected for C- and L-bands. While the short p ulse length minimized the altitude affected by **clutter** from the surface sidelobes, the bandwidth **effect** depended 011 the s(0l'll 1. On one hand, the surface clutter is inversely proportional to the pulse bandwidth. which implies that **a** large bandwidth setting would minimize the altitude affec ted by the surface return. 011 the other hand, the signal-to-noise ratio (SNR) **is** inversely proportional to the bandwidth. This implies that for storms with **a** significant ar nour t of expected total attenuation from the top **Of** the storm to that altitude w here the **Sill'faCC** clutter t akes over, **i.e.** for storms where the SNR **would** become uncomfortably **low,** the narrow bandwidth would still maximize the SNR. X- SAR w a s operated with **a** 40 μsec pulse length and a 9.5 MHz bandwidth. No bea m steering **was** used. The (lowest) pulse repetition frequency, 1.24l KHz, still produced er rough pulses to reduce the fading effects, without introducing any range ambiguities or pulse shadowing effects, and while saving on data storage.

Setting the receiver gain values was less straightforward. ()]I one hand, the mere detection of l'sill depends only 011 the SNR, with the accuracy of the quantitative *estimation* of the rain reflectivity improving **as** the dynamic range of the quantized return increases. 011 the other ha nd, the fact **that** the return from the **Sul'race!** can be **as** much as 55 dB greater than the return from 0.5 111111]1^{-1} rain (Okamoto et al., 1988), **and** would therefore most probably drive the 8-bit (SIR-C) or 6-bit (X- SAR) quantizers into non-linearity, places an upper-bound constraint 011 the receiver gain: **as** the gain **is** increased, the increasing echo from the surface would eventually strongly saturate the receiver. It w a s therefore decided to s e t the receiver gain so that tile return from the top **of** the stron gest expected convective storm was near the top **of** the dynamic range o f the quantizers. This would not avoid saturation by the surface return, but it would still allow one to measure low rain-rates.

I) 'T' 34.55 from S1{1,-1 produced **clear** but somewhat disappointingly weak reflectivity profiles from several rain showers within the outer rain band of T ropical Cyclone Odille in the Indian Ocean 011 April]], 1994, around 12:42 GMT. The **1,-** and C-band radar parameters

were incorrectly set during DT 45.5 from SRL-2. DT's 54.0 and 103.0 from SRL-2 produced the most spectacular data. Both were performed over Typhoon Seth in the Western Pacific, DT 54.0 on October 3, 1994, around 17:14 GMT, and DT 103.0 on October 6, 1994, around 18:14 GMT. Both contain localized echos from several convective cells as well as extended returns from stratiform rain. The remainder of this section will concentrate on describing one stratiform and two convective cases.

Fig. 1a shows the GMS IR image from October 6 at 17:32 GMT, overlaid with the Shuttle track during data take 103.0. The black cross towards the bottom left of the track marks the location of a convective cell that produced the reflectivities shown in Fig. 2. Since the GMS image preceded the data take by about half an hour, one expects the brightness temperatures to have changed a little by the time of the Shuttle pass. Fig. 2 shows the measured VV effective radar reflectivy factors at the three frequencies. The tick marks on the vertical axes are spaced 1 km apart, the ones on the horizontal axes 3 km apart. The surface is colored navy blue. No surface clutter subtraction was performed on the SIR-C reflectivities because the surface return was saturating the receiver too strongly. However, we were able to subtract the clear-air surface return from the X-SAR data, although some residual noise was unavoidable. Note that while C- and X-bands are plotted using the same color scale, a different scale was used for L-band. The discrepancy in the C- and X-band reflectivities, on one hand, and the L-band reflectivity, on the other, is due largely to the difference in the along-track antenna beam widths: while the 3-dB beam width is 0.25° at C-band and a comparable 0.15° at X-band, it is 1.1° at L-band. Thus, the obviously significant along-track variation of the intensity explains the large-scale difference between X/C- and L-bands. The along-track variation of the intensity also strongly suggests that the rain was very non-uniform across track too. While a gain corresponding to the nominal 5° - 6° across track 3-dB beam widths was assumed to produce these images, it is much more likely that the rain echo was produced by precipitation occupying a fraction of the corresponding space. In fact, since the along-track dimension of the "pockets" producing the strongest rain reflectivities manifestly did not exceed 2 km, one can reasonably assume that the same must have been true of the across-track dimension. Since this would correspond to a 0.5° ocean width one can therefore conclude that the measured reflectivities are very likely about $10 \log_{10}(5/0.5)$ 10 dB too low because of partial beam-filling.

While no significant cross-polarized return was measurable in this slice of data, the return from the convective cell marked by the black cross on the upper portion of the track in Fig. 1a did produce a distinct VH return at C-band. Fig. 3 shows the C-VV, L-VV and C-VH reflectivities. The tick marks are as in Fig. 2, the color scale for C-VV and L-VV are also as in Fig. 2, but the C-VH reflectivities were plotted with a different color scale to enhance what appears to be the return from melting ice particles. Leakage from the V channel can be ruled out since the strong VV returns from the lower altitudes do not appear in the VH data. Such signatures were observed routinely during the Convection and Precipitation/Electrification (CaPE) project in Florida, and were found to be due to the

melting of denser ice particles. While the returns in Fig. 2 are considerably weaker than those observed during CaPE, this is most likely due to the severe beam filling problem as well as the much greater distance between the radar and the clouds.

Fig. 1b shows the GMS IR image from October 6 at 17:32 GMT, overlaid with the Shuttle track during data take 54.0. The black "TOSS about two-thirds of the way up along the track marks the location of the region of stratiform precipitation within the outer edges of Typhoon Seth that produced the reflectivities shown in Fig. 4. The four panels in that figure show the measured VV reflectivities at the three frequencies as well as the C-VH reflectivity. The tick marks are as in the previous two figures, as are the three ("0101" scales (X/C-VV, L, and C-VH). As before, no surface-subtraction was performed except for the X-band data (where subtracting the clear-air surface return is necessary because of the long illuminating pulse).

There are several interesting features in the stratiform image, Fig. 4. In all panels, the appearance of the "melting band" is striking. While this observation is not new (the so-called "bright band" has been studied off and on over the last 50 years), these observations are not only the first reports from a spaceborne radar, but they are the first collected simultaneously at three frequencies and at two polarizations. The rapid increase in signal intensity responsible for the banded appearance is due largely to the change in the index of refraction as ice begins to melt (Austin and Bemis, 1950; Browne and Robinson, 1952; Newell and Geotis, 1955, to name a few). The magnitude of this effect, however, is governed not only by the transition to a liquid having a much greater index of refraction, but also by other factors such as the kind of icy hydrometeor, any growth (accumulation of mass) of ice just before melting, and changes in fall speed as melting proceeds. Specifically, icy hydrometeors range in densities from 0.05 to 0.9 g cm^{-3}. Particles having lower densities are usually ice crystals and snowflakes, while hydrometeors having higher densities are the more compact ice particles such as hail and graupel. These differences are important with respect to the signals because, for example, snow and crystals usually fall at a rate of around 1 m s^{-1} while the denser particles can reach terminal fall speeds of several meters per second. Consequently, snow and ice can have a substantial increase in mass (and therefore, radar reflectivity) just before melting by the processes of vapor deposition and the accretion of supercooled (subfreezing) cloud droplets. Moreover, snow and ice crystals tend to clump as they fall so that they can become low density aggregates having quite large dimensions of one to several centimeters. On the other hand, the relative change in mass of the higher density particles is usually considerably smaller because their substantial terminal velocity assures a rapid passage through the thin layers of supercooled cloud. In addition, these hydrometeors rarely aggregate.

Furthermore, the melting processes of these two types of hydrometeors are different. The denser particles tend to form a film of surface liquid with melting of the ice continuing inside this liquid shell. A horizontally oriented ring of liquid water can form around the middle of the hydrometeor before melting is completed. Snow, on the other hand, begins by

first wetting the outer, most exposed crystals so that the snow at first acts like a clump of randomly oriented dipoles (e.g., see the discussion in Jameson, 1989). As melting proceeds, however, this three- dimensional asymmetric structure collapses into a more two dimensional pancake of loosely bound water drops which finally breaks apart once the icy structure looses its integrity. Moreover, because the raindrops fall with their largest dimensions oriented horizontally, they generate very little cross-polarized return unless they are several mm in diameter (Jameson and Durden, 1996), an infrequent occurrence in this type of rain. Furthermore, whereas the terminal fall speed of the denser ice may show little to modest increases in fall speed, the drops from the melted snow fall considerably faster than the original flakes. As a consequence, between these two types of hydrometeors, differences appear in the signals associated with the melting layer. In particular, less dense particles tend to form very shallow (in depth), well-defined radar bright bands (as in Fig. 4) because the melting occurs in a thin region as a consequence of the slow fallspeed of the snow. Significant cross-polarized signals occur at the melting level where the wet crystals act like randomly oriented wet dipoles. Once the melting is completed, however, the cross-polarized signals disappear with the formation of the raindrops. Signals from the melting of denser hydrometeors (as illustrated in Fig. 3), on the other hand, tend to be weaker in part because the melting occurs over much greater depths (because of the larger fallspeed and different melting process), and the cross-polarized signals tend to be much reduced because, unlike snow, these particles usually lack significant three dimensional asymmetry during melting.

So what do the structures in Fig. 5 tell us? Beginning with the C-band vertical polarization panel at the top, a thin melting layer is clearly evident. Above, there is a hint of precipitation, while below shafts of rain are clearly evident. In the cross-polarized channel at C-band (C-VH), cross-polarized signals are evident with little if any signal above or below the melting layer. This is precisely the scenario anticipated for melting snow and ice crystals, and we can conclude with good confidence that the 0°C isotherm lies near 5 km above the ocean surface, a common height above warm tropical oceans. In addition, as one might expect because of the higher frequency, it appears that the X-band is somewhat more sensitive than the C-band to the presence of ice above 5 km, yielding clear evidence of a band of snow descending from much greater heights. The sudden increase in speckle in X-band signals below the melting level may, in part, also be the result of depolarization by the precipitation in the melting layer at this higher frequency. While the increased sensitivity at X-band may not be too surprising, it is rather amazing to see how readily the melting layer is detected at L-band. Since L-band is not particularly sensitive to liquid water such as raindrops, such a strong signature at the melting layer must not only be a response to the change in the index of refraction, but must also be due to the presence of very large particles of several centimeter diameter. Very few hydrometeors besides hail reach these dimensions. Yet it is unlikely that these observations involve hail which can only come from highly convective storms. Instead we must conclude that the particles are very large aggregates of moist, melting snow. In principle more quantitative estimates of the particle sizes should be possible by considering the ratios of these measurements at different frequencies. However, the beam dimensions

at the different wavelengths are so disparate that such studies could be very misleading. Nevertheless, it is reasonable to conclude that we **arc** not only looking at melting ice crystals but also at very large melting snowflakes, and that the melting level is at 51<111.

Although independent confirmation of these observations during the experiment was not possible, they are in agreement with similar observations in different settings using different radars **a s** indicated in Fig. 5. A profile through the melting level in Fig. 4 is illustrated in Fig. 5a. The structures are quite similar to those observed using the NASA/JPL AR MAR airborne radar that flew over **a** melting layer **associated** with a forming tropical cyclone in the tropical Western Pacific two years earlier. Note the similar structures in both the linear depolarization ratio [defined by LDR $= 10 \log_{10} (Z_X / Z_C)$, where Z_X and Z_C are the radar reflectivity **factors** at cross- and co-polarization, respectively] and the reflectivity **factor,** Z. Finally, ground-based NCAR/CP-2 **vertically** pointing radar measurements in stratiform precipitation in Florida are shown in Fig. 5c. While exhibiting similar features, they are displaced downward by about 1 km. Particularly noteworthy **is** the increase in the downward fallspeed of the scatterers **as a** consequence of melting. In fact, one can estimate **the** mass weighted mean size of the drops assuming that the vertical air motion in this kind of situation is negligible compared to the fallspeed **of** the hydrometeor (which is often the case in **stratified** systems after melting has occurred). Under this assumption, a fallspeed **of** 7 **III s**$^{-1}$ implies a mass weighted drop diameter of around 2.2mm (Jameson, 1993), a very reasonable value. Thus, when such structures exist, spaceborne observations of these features can be used to derive reasonable estimates **of** the height of the melting level and even reasonable estimates **of** the size **of** raindrops under the right conditions. This **is** important, for example, because when attempting to derive quantitative estimates **of** rainfall from radiometric and radar measurements, it **is** important to know something about the size **of** the particles and the depth of the region likely to contain rain. For radiometers this **is** important because rain **is a** strong emitter of microwave radiation, while for radars, it **is a** strong absorber **of** microwaves at higher frequencies. Both processes depend on the size of the raindrops and the extent **of** the rain.

While it **is** most interesting to study the echoes due to precipitation, the surface returns proved quite interesting in themselves. Fig. 8 shows the time series of a typical **raw** C-VV return from the surface. Receiver saturation makes it impossible to convert the echo power to an accurate **sul'face** backscattering coefficient. But one can still analyze the statistics **of** the surface at the three frequencies, in clear **air** and under rain. Table 1 summarizes the results about the behavior of the **surface** Z-factor, with a **surface** echo **classified as** coming from "clear air" conditions if no C-VV echo between 2 **Ii III** and **6** km above it exceeds 22 dBZ. The three data segments that were analyzed correspond to track segments surrounding those shown in figures 2, 3 and **4.** Each consists of 1500 independent surface Z-**factor** samples, each sample consisting of the **average** power of 32 consecutive raw echoes. Laboratory experiments (Poon et **al**, **1992,** and Tsimplis, 1992) have shown that surface **waves** with wavelengths on the **order of** 10 cm do get damped by rain, mostly due to turbulence, the damping rate increasing

with rain intensity, yet that rain-induced ripples increase the spectral density of the ocean surface slope in the 1-cm scale as rain intensity increases. In our empirical analysis, while the surface does appear to be between 1 and 2 dB brighter under clear air than under rain, even at L-band where the attenuation of microwaves due to rain is certainly negligible, the more striking effect is the significantly increased variability in the surface reflectivity under rain, once again even at L-band. Decreased average reflectivity at nadir under rain is consistent with a rougher surface, due to falling drops and/or the presence of downdrafts. The fact that the increase in the variability is more pronounced in the convective cases than in the stratiform case, and indeed that the surface reflectivity under rain can exceed that in clear air (not on average but in a sufficient number of occurences to affect the statistics of convective case 1 at C-band) is consistent with an ocean surface that can become substantially rougher but that can also become significantly calmer due to damping of surface waves by heavy rainfall.

3 Side-Looking Observations

As part of the experiment, side-looking data over rain were acquired on data takes 13.4, 46.3, 66.6, 72.9, 140.4, 147.8, and 149.1 on SRL-1. On SRL-2, side-looking data over rain were acquired on data takes 13.4, 77.5, 114.0, 114.6, 119.0, 141.5, and 157.5. Because of the side-looking geometry, quantitative interpretation is challenging. Previous side-looking SAR imagery of rain over the ocean has been interpreted in terms of the effects of wind and rain on the ocean surface (Atlas, 1994). These analyses, however, have dealt only with single polarization and single frequency data. The multiple frequencies and polarizations used in the SIR-C/XSAR data reduce the ambiguity in interpreting the data

DT 13.4 from SRL-1 is of particular interest because it captured an extensive rain area using mode "16X", giving the full scattering matrix at L- and C-bands. Fig. 9 shows an example of three-frequency VV polarization imagery from this data take. At L-band, the variability in backscatter is likely to be entirely controlled by ocean σ^o variations. The attenuation in rain at L-band is much less than 1 dB, even for rainrates well over 100 mm/h. Also, rain backscatter is expected to be small relative to the return from the ocean. At C- and X-bands, interpretation becomes more complicated, since both attenuation and scattering in rain could be significant. A comparison of the three images in Fig. 9 shows that in many areas the brightness of the image varies similarly at all three frequencies. However, a few areas appear dark at L-band but bright at C- and X-bands. These are noted as A-D in Fig. 10. Also, although the "hole" E is dark in all three images, the area just to the left becomes bright at C- and especially X-bands. Variation in brightness with frequency is a common phenomenon, appearing not only in Fig. 9 but in many other data takes as well. The linear depolarization ratio at C-band helps understand this phenomenon better. Indeed, as discussed in the previous section, LDR is often used in radar meteorology to identify regions

with ice particles. In the data at hand, the areas which are dark at L-band but bright at C-band have large LDR (-12 dB), suggesting that these are convective regions, producing heavy rain. At L-b and, the return is from the ocean surface and may be reduced in strength by modification of the ocean surface by rain. As was mentioned at the end of the previous section, damping of ocean waves by rain has been observed in controlled experiments (Poon et al, 1992, and Tsimplis, 1992), and its effect on SAR ocean imagery has already been hypothesized (Atlas, 1994). The large LDR may be produced by scattering from ice, while the large CVV return may be a combination of scattering from ice and heavy rainfall.

Also of interest in these data is the behavior of the phase difference between the HH and VV return. This difference provides information about the scattering mechanism and has been studied previously in polarimetric SAR observation of vegetation (Durden et al, 1989). Over most of our imagery the HH VV phase is approximately zero but becomes non-zero in some rows. In Fig. 9, for example, the phase difference at C-b and is up to 30 degrees in the areas which are dark at L-band and bright at C- and X-band (A-1) in Fig. 10). This is consistent with "double b ounce" scattering, in which the transmitted wave forward-reflects from the surface and then reflects from rain back to the radar. This mechanism would require a smooth ocean, such as might be produced by rain-damping of ocean waves. The double-bounce mechanism is analogous to a dihedral corner reflector, which produces a 180 degree phase shift between HH and VV return. The maximum phase difference of around 30 degrees observed here suggests that the double bounce mechanism is contributing to the total return but is not dominant. Another region of interest in Fig. 9 is the elongated dark area in the lower right (F in Fig. 10), which has a C-band phase difference up to 50 degrees. This area is dark at all three frequencies, indicating that the rain rate is light. A moderately smooth ocean would be needed to explain the signature. However, in this case the rain is likely too light to be causing wave damping. Instead, it could be an area with low winds.

In addition to data takes over tropical oceans, SRL-1 serendipitously captured several rain cells over the Amazon rain-forest. These data are particularly interesting because while interpretation of SAR imagery of rain over the ocean is complicated by the possibility of backscatter and attenuation in rain, as well as the variability of the ocean σ^o itself, images of rain over the Amazon cannot suffer from any significant surface σ^o variability (assuming that rain does not strongly affect back scatter from trees). Fig. 11 shows three-frequency imagery of rain cells over the Amazon during DT 103.6 from SRL-1. At X-band the rain cells show up as bright areas, immediately followed by large dark areas at increasing range. At C-band, no brightening is visible, but some dark areas can be seen in the same location as the dark areas at X-band. At L-band neither bright nor dark areas are visible. At all three frequencies the transmitted wave is both scattered and attenuated by the rain. However, at L-band, both effects are small. At C-band the attenuation is large enough to reduce the observed σ^o by the two-way loss through the rain. The rain backscatter is small relative to the tree-top backscatter and is not seen. At X-band the backscattering from rain is large enough that it can be seen above the cross section of the tree tops. However, as range increases, the

signal backscattered from both surface and rain is attenuated strongly. To interpret these observations quantitatively, we consider scattering from a random medium over a reflecting surface. Scattering consists of the components illustrated in Fig. 12: direct backscatter from the random medium, backscatter from the surface, direct-reflected interaction of the surface with the random medium, and backscatter from the random medium, reflected by the surface. The total ocean σ^o is given by

$$\sigma^o = \sigma^o_s + \sigma^o_d + \sigma^o_{dr} + \sigma^o_{dr} \tag{1}$$

where the subscript s denotes surface, d denotes direct from rain, dr denotes direct-reflected, and r denotes reflected. Note that each term includes both scattering by the surface and/or random medium and also attenuation due to the intervening random medium. As mentioned above, the dr term can provide a large phase shift between HH and VV. This model has been used extensively in modeling SAR imagery of vegetation. In the case at hand, the random medium represents rain rather than vegetation, while the surface is the ocean. For vegetation, this model has typically been implemented using the Distorted Born Approximation (DBA) and assuming that the surface is only slightly rough, so that the dr and r terms use only the specular or coherent component from the surface. The DBA assumes that the scatterers in the medium see the attenuated field. This assumption is also used in the radar equation of radar meteorology and should apply to our case. The assumption of a slightly rough surface, however, cannot be justified for the ocean at the frequencies used here. Hence, both the dr and r terms will be much more complicated than in the vegetation case, requiring integration over the scattering pattern of the surface. This has, in fact, been carried out previously for the r term in the case of radar observations of rain over the ocean at nadir and turns out to be quite complicated (Meneghini and Atlas, 1986). Their work attempted to use the r term, also called mirror image return, to profile rain. For the case of backscattering from rain over a rainforest, the model can be simplified to include only the surface and direct backscatter terms. A simple model of the backscatter from a rectangular rain cell over the rain-forest was thus constructed. The model cell is 4.5 km in altitude and 4 km wide (cross-track direction) and has a rainrate of 40 mm/hr. Fig. 13 plots the observed and modeled σ^o versus rain range. The model duplicates the observation quite well, supporting our interpretations. Rain cells such as these can be found in many of the SIR-C/X-SAR data takes over the Amazon rainforest.

4 Conclusions

In summary, the SIR-C / X-SAR mission's data over rain storms have successfully produced the first multi-polarization and multi-frequency measurements of precipitation from space. Rainfall was clearly detectable even at L-band. We were able to estimate rainrates from the C- and X-band returns. Melting hydrometeors were clearly detectable in the cross-polarized C-band echoes from stratiform as well as convective systems, much as one would expect given past ground and air-borne measurements.

The data **also** confirm previous observations that rain and wind effects can produce large variations in **30°** -- 5 0°-incidence-angle sea surface backscatter. At nadir, however, the ocean surface backscatte ring coefficient was not **a s** dramatically affected by the rain storm, although the backscattering coefficient did decrease while **its** spread was significantly larger than that **of** the clear-air measurements, even at L-band.

Finally, several areas with significantly non-zero HH-VV phase differences and apparently lighter rainfall were observed in the ocean images.

5 A cknowledgements

6 References

Atlas, D. A., 1994: Origin of storm footprints on the sea by synthetic aperture radar, *Science* 266, 1364-1366.

Austin, P.M., ant] Bemis, A.C., 1950: A quantitative study of the "bright band" in radar precipitation echoes, *J. Meteor.* 7, 145- 151 ,

Browne, I.C., and Robinson, N.])., 1952: Cross polarization of the radar melting band, *Nature* 170, 1078-1079.

Durden, S. 1,., van Zyl, J. J., ant] Zebker, 11. A., 1989: Modeling and observation of the radar polarization signature of forested areas, *IEEE Trans. Geosci. Remote Sensing* 27, 290-301.

Jameson, A .R., 1989: The interpretation and meteorological application of radar backscatter amplitude ratios at linear polarizations, *J . Atmos. Oceanic Technol.* 6, 908-919.

Jameson, A.]{., 1993: The meteorological parametrization of specific attenuation and polarization differential phase shift in rain, ,*J. Appl. Meteor.* 32, 1741-1750.

Jameson, A .R., and Durden, S.L., 1996: A possible origin of linear depolarization observed at vertical incidence in rain, *J. Appl. Meteor.* **35, '271-277.**

Meneghini, R., and Atlas, D. A., 1986: Simultaneous ocean cross section and rainfall measurements from space with a nadir-looking radar, *J. Atmos. Ocean. Tech.* **3,** 400-413.

Newell, R.E., and Geotis, S. G., 1955: **Met** corological measurements with a radar provided with variable polarization, *Weather Research Tech.* Note No. 8, Dept. or Meteorology, Massachusetts Institute of' Technology, 12 pp.

Okamoto, **K.,** Awaka, J., and Kozu, 'J'., 1988: A feasibility study of rain radar for the tropical rainfall measuring mission: (i. A case study of rain radar system,

1'0011, Y.]<., Tang, S., and **Wu, J., 1992:** Interactions between rain and wind-waves, *J. Phys. Ocean.* **22, 97&987.**

Tsimplis, M.N., 1992: The effect of rain in calming the sea, *J. Phys. Ocean.* **2 2,** 40'1-412.

Figure captions

Figure 1: GMS IR images of Typhoon Seth with the Shuttle tracks overlaid: (a) October 6, 1994, 17:32 GMT the **two crosses** mark the **location** of the convective cells in Fig. 2 and **3**; (b) October 3, 1994, 17:32 GMT - the cross marks the location of the stratus in Fig. **4.**

Figure 2: Along track cross-section **of** the radar reflectivities from **a** convective cell in Typhoon Seth. Vertical tick marks indicate 1-km intervals , horizontal ones 3-km intervals. The surface **is** represented in navy blue. Note the two different **color** scales for the X/C and L-bands.

Figure 3: Along track cross-section **o f** the radar reflectivities from **a** second convective cell in '1'])110011 Seth. Vertical tick marks indicate 1-km intervals, horizontal ones 3-km intervals. The surface **is** represented in navy b lue. The color **S['ales** for the C-VV **and** L-bands are as in Fig. 2. C-VH is represented using the third ('**0101**" scale shown at the bottom ,

Figure 4: Along track cross-section of the radar reflectivities from stratiform precipitation in Typhoon Seth. Vertical tick marks indicate 1-km intervals, horizontal ones 3-km intervals. The surface **is** represented in navy blue. The three different color scales for X/C-VV, L, and C-VH are as in Fig. 2 and 3.

Figure 5: Profiles of radar parameters till'OHF;ll melting layers as **a** function **of** height above the surface **011** three different **occasions** using three different radars: (a) Spaceborne SIR - C/X-SAR measurements **of** the linear depolarization ratio (LDR) at C-band and the radar reflectivity factors **(X)** at L- C- and X-bands associated with Typhoon Seth; (b) Airborne ARMAR measurements including the profile of particle vertical velocities (v= fallspeed -| vertical air speed) in a developin g tropica l storm over the Western Pacific; **(c)** Measurements in Florida using the ground-based NCAR CP-2 radar.

Figure 6: Reflectivity profiles through the convective cell in Fig. 2.

Figure 7: Typical quantized raw C-VV echo from the surface.

Figure 8: Three-frequency VV images from 1) '1' 13.4 during S1{1,-1.

Figure 9: Schemati c showing the location of features in the rain cell **of** Fig. 9.

Figure 10: Three-frequency VV images **of** rain cells over the Amazon from 1)T 103.6 during SRL-1.

Figure 11: Scattering mechanisms from **a** random medium over a reflecting surface.

Figure 12: Observed **and** modeled dependence of σ^0 versus range for an Amazon rain cell in 1) '1' 103.6 .

|	$10\log_{10}(Z_s - 2\sigma)$	$10\log_{10}(Z_s - \sigma)$	$10\log_{10}(Z_s)$	$10\log_{10}(Z_s + \sigma)$	$10\log_{10}(Z_s + 2\sigma)$
convective 2 - rain - L-VV	48	56.8	59.6	61.2	62.4
convective 1 - rain - L-VV	45.1	57.6	60.5	62.2	63.4
convective 2 - rain - C-VV	47.3	58	60.8	62.5	63.7
convective 1 - rain - C-VV	57.3	60.9	62.8	64.1	65.1
convective 2 - clear - L-VV	59.2	60.6	61.7	62.6	63.3
convective 1 - clear - L-VV	60.9	61.5	62.1	62.6	63
convective 2 - clear - C-VV	61	62.4	63.5	64.4	65.1
convective 1 - clear - C-VV	62.5	63.2	63.8	64.3	64.7
stratiform - rain - C-VV	54.8	58.3	60.2	61.5	62.5
stratiform - rain - L-VV	56.8	59.3	60.9	62	62.9
stratiform - clear - C-VV	60.3	61.1	61.7	62.3	62.7
stratiform - clear - L-VV	60.7	61.4	61.9	62.5	62.9

Table 1: **Statistics** of the surface reflectivity Z_s, in dBZ
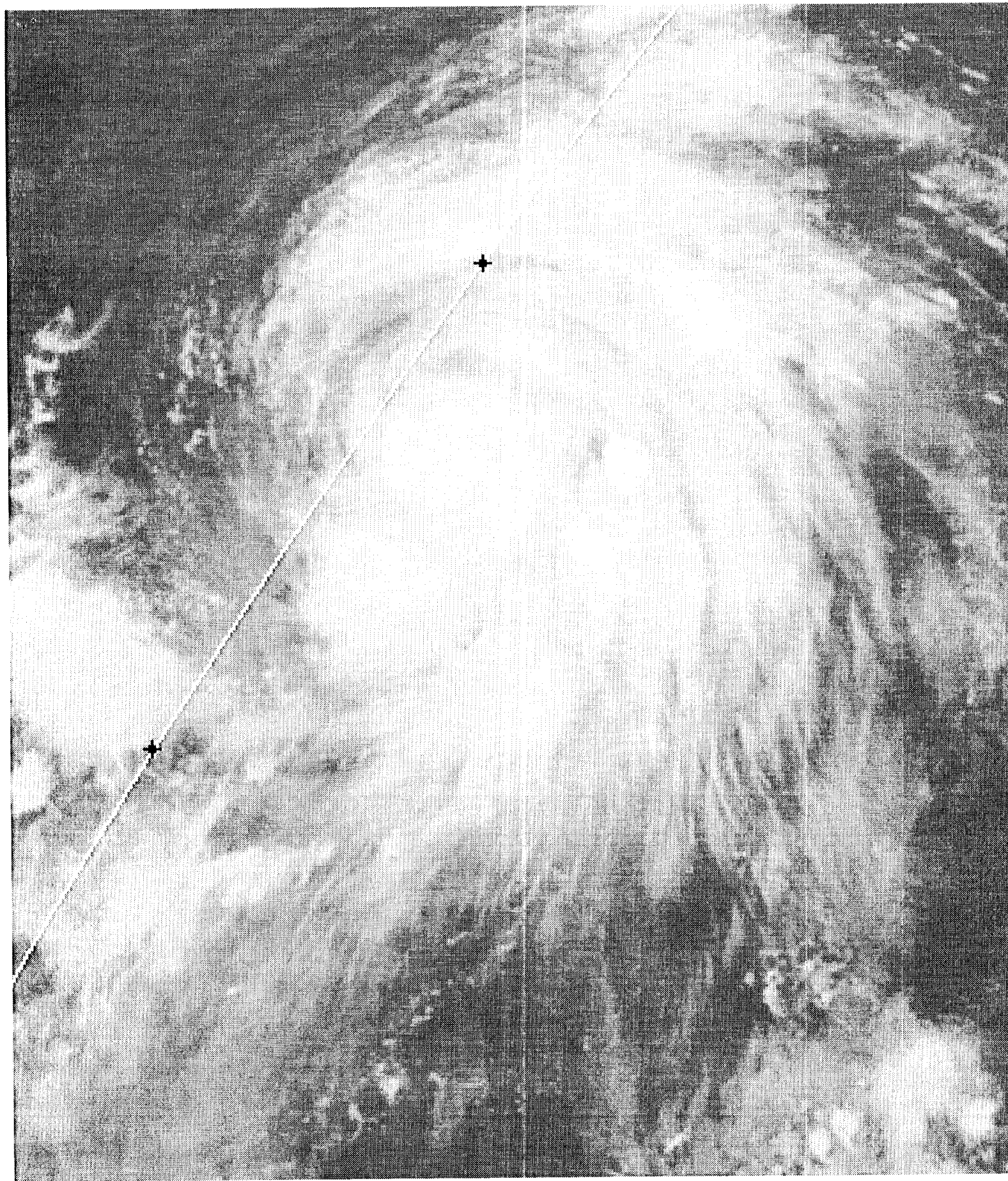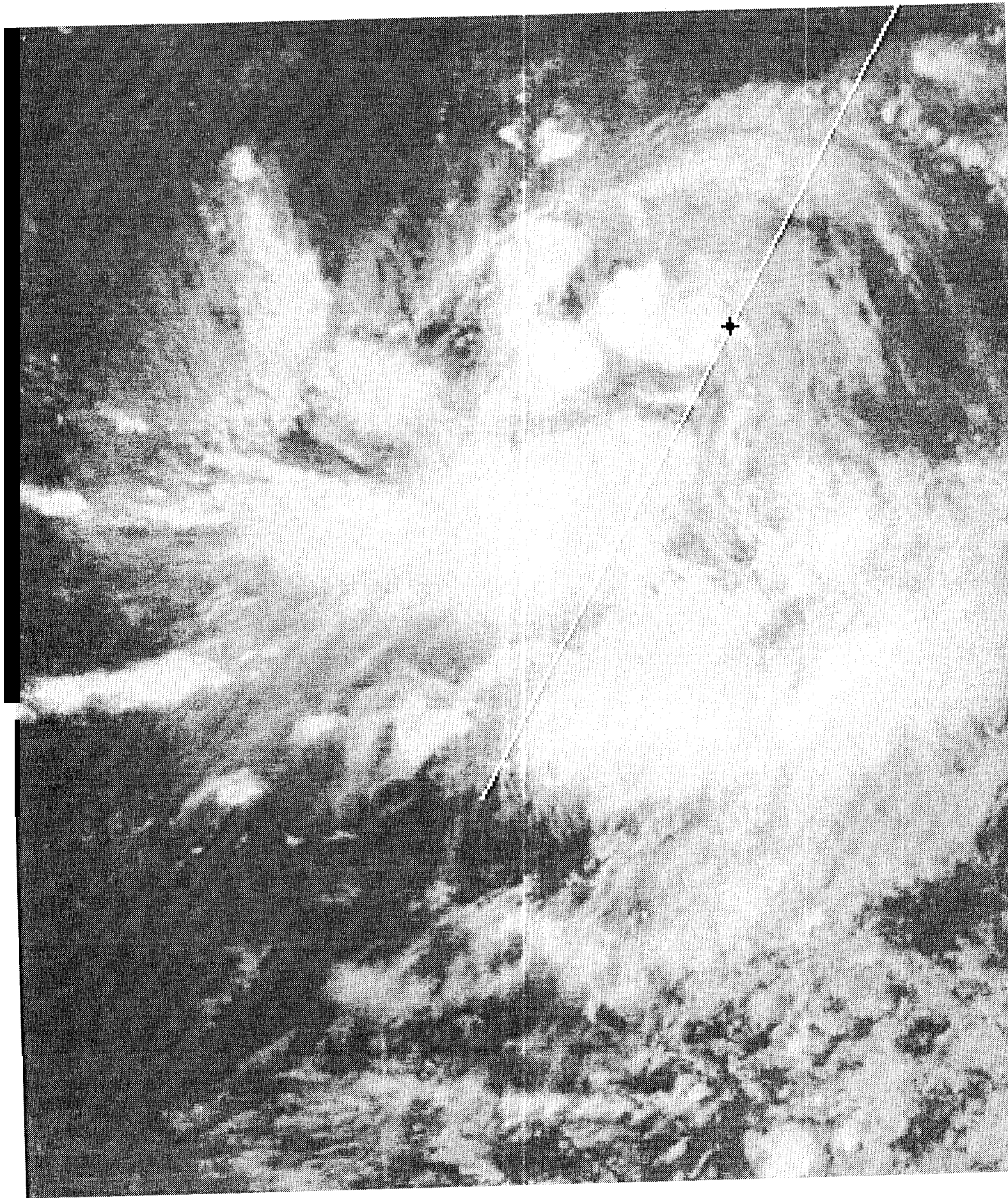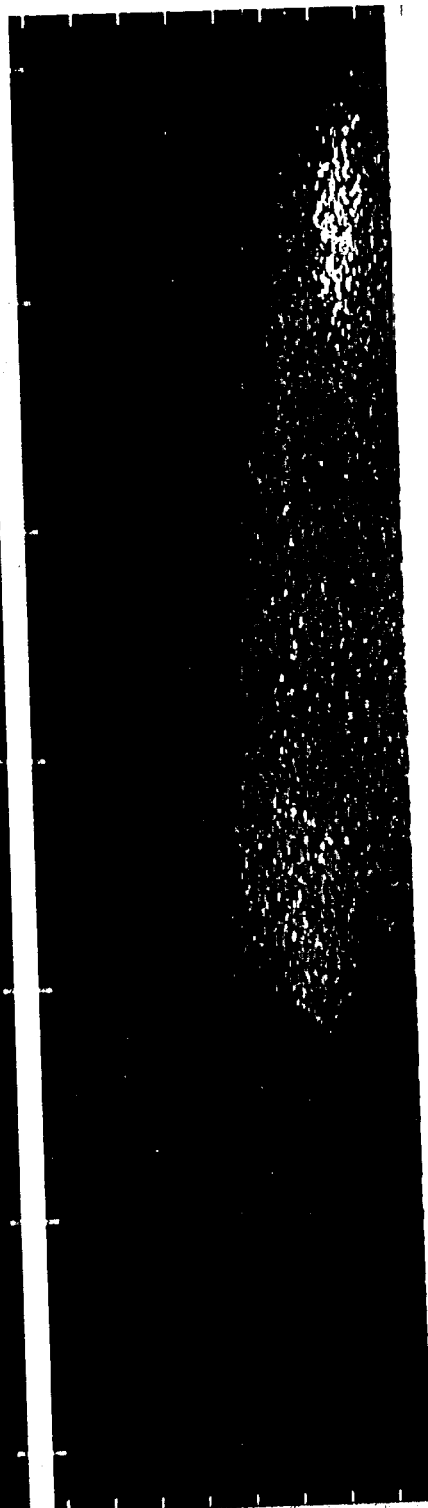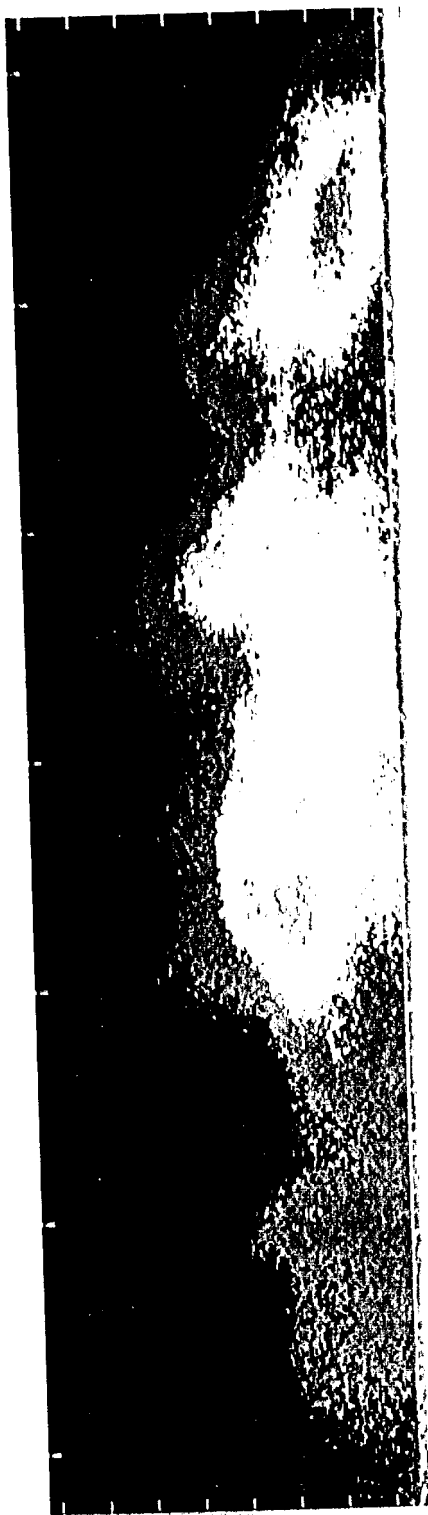
M
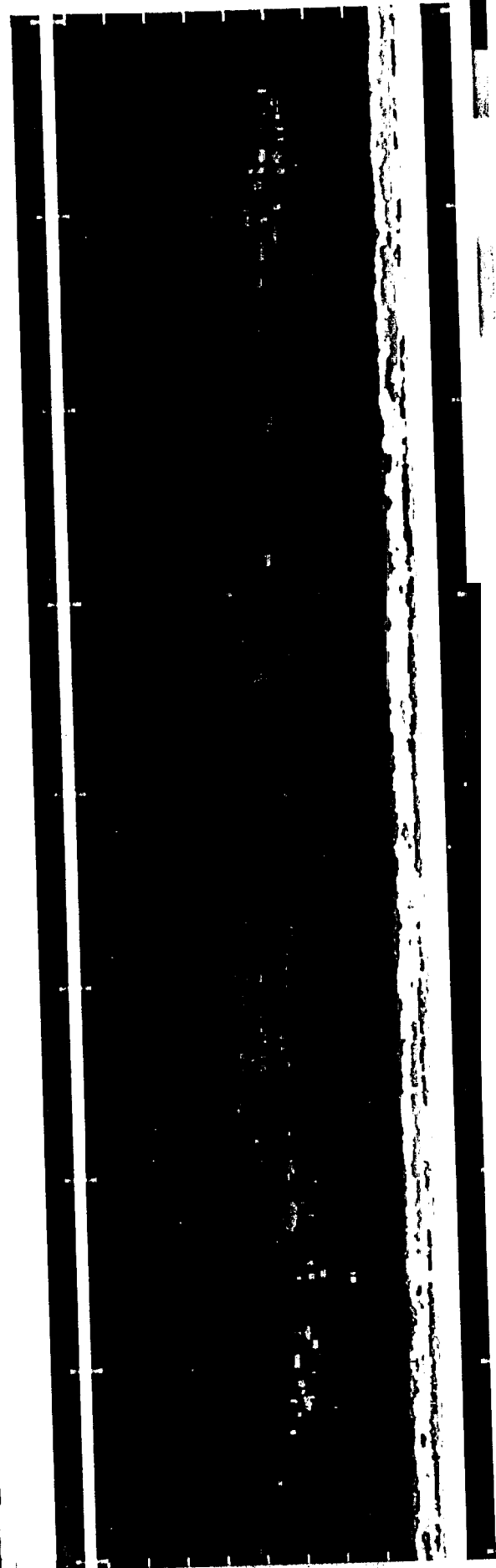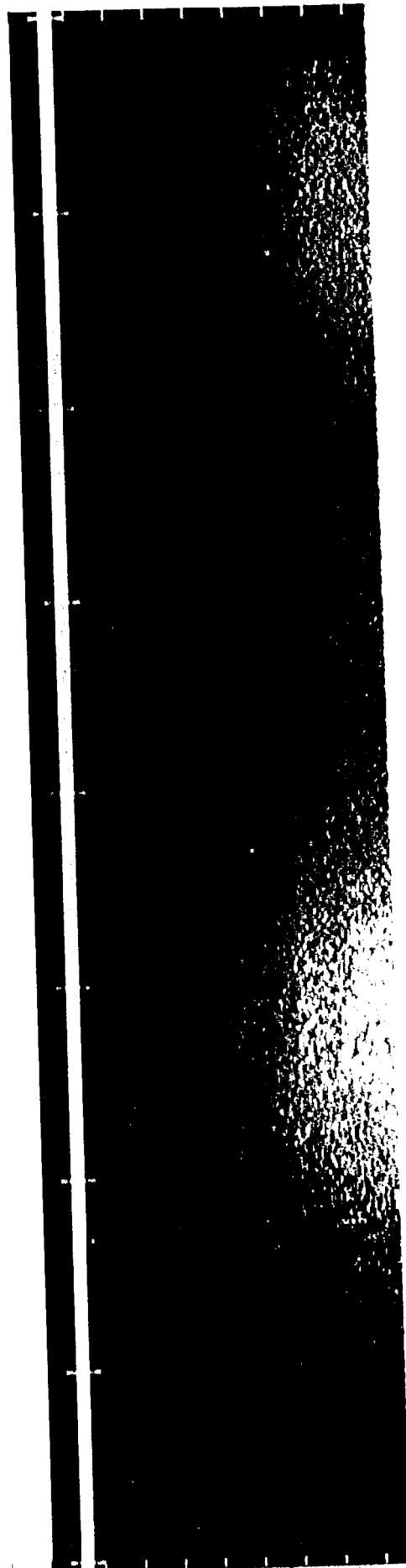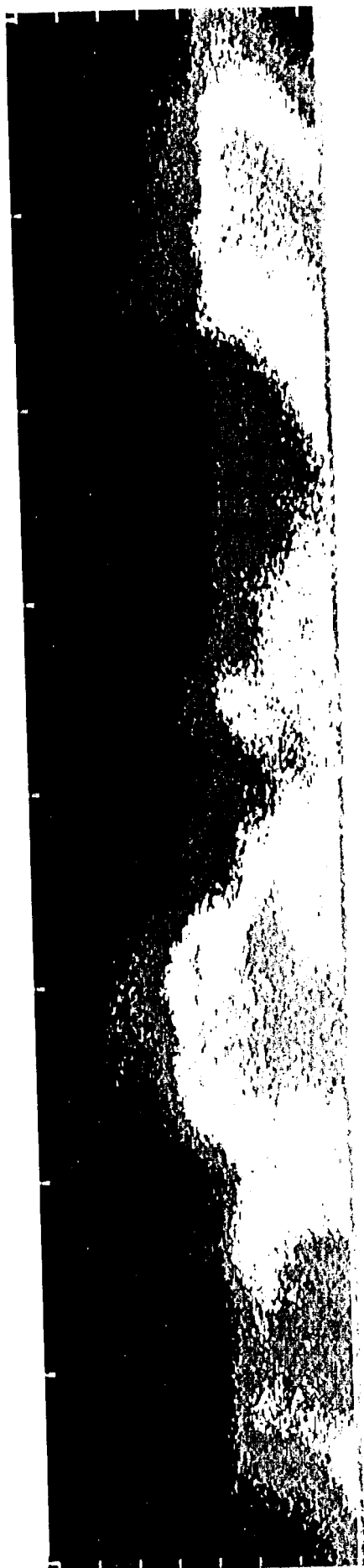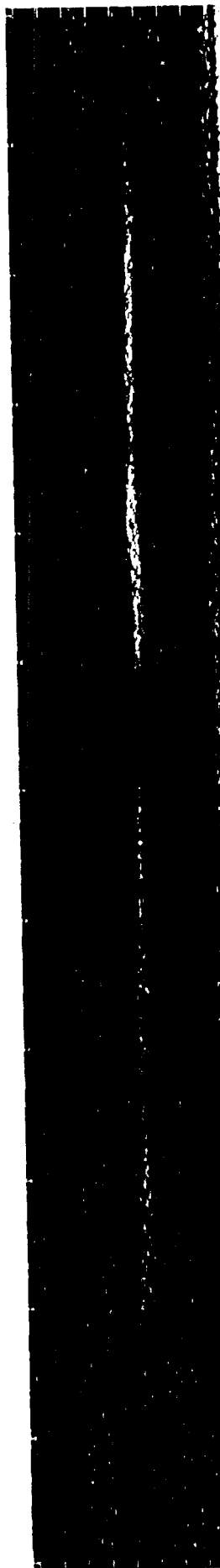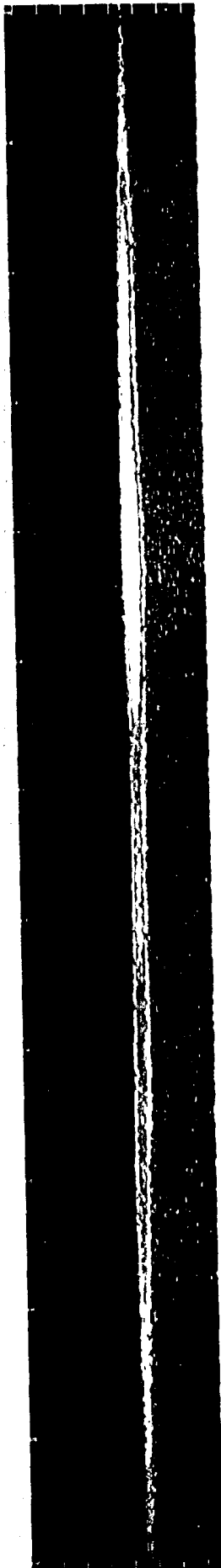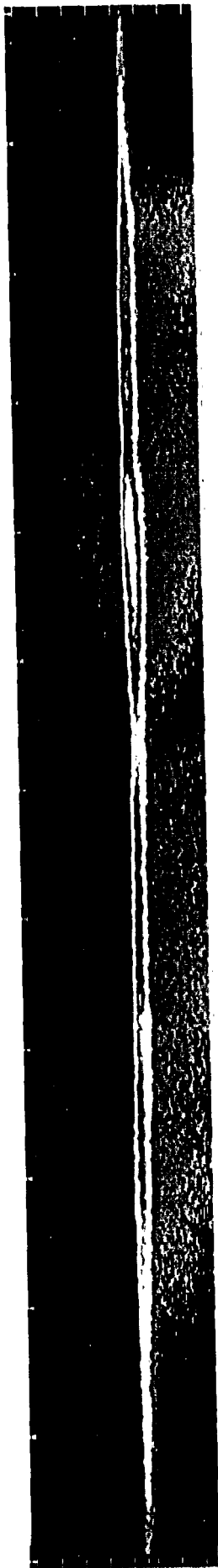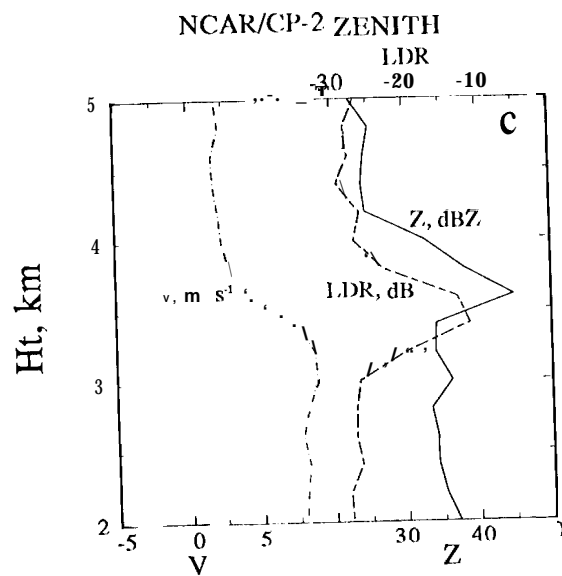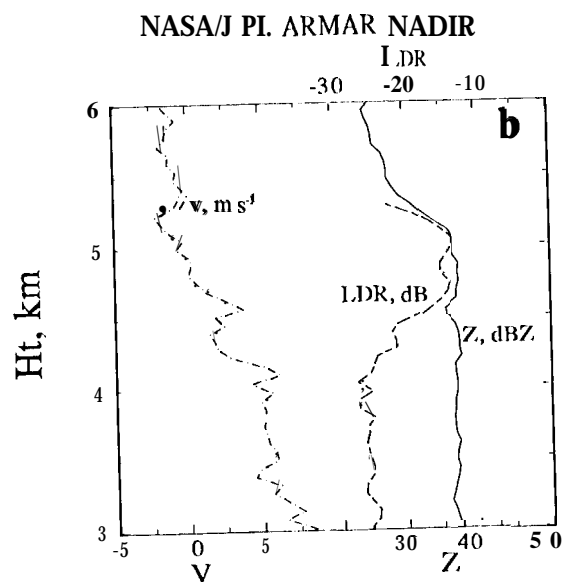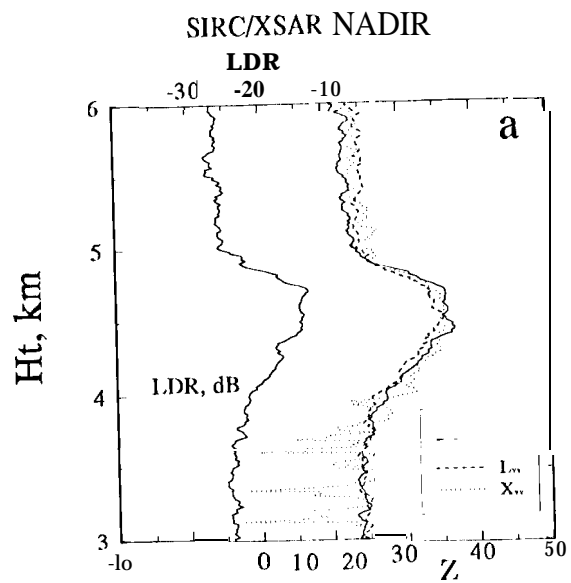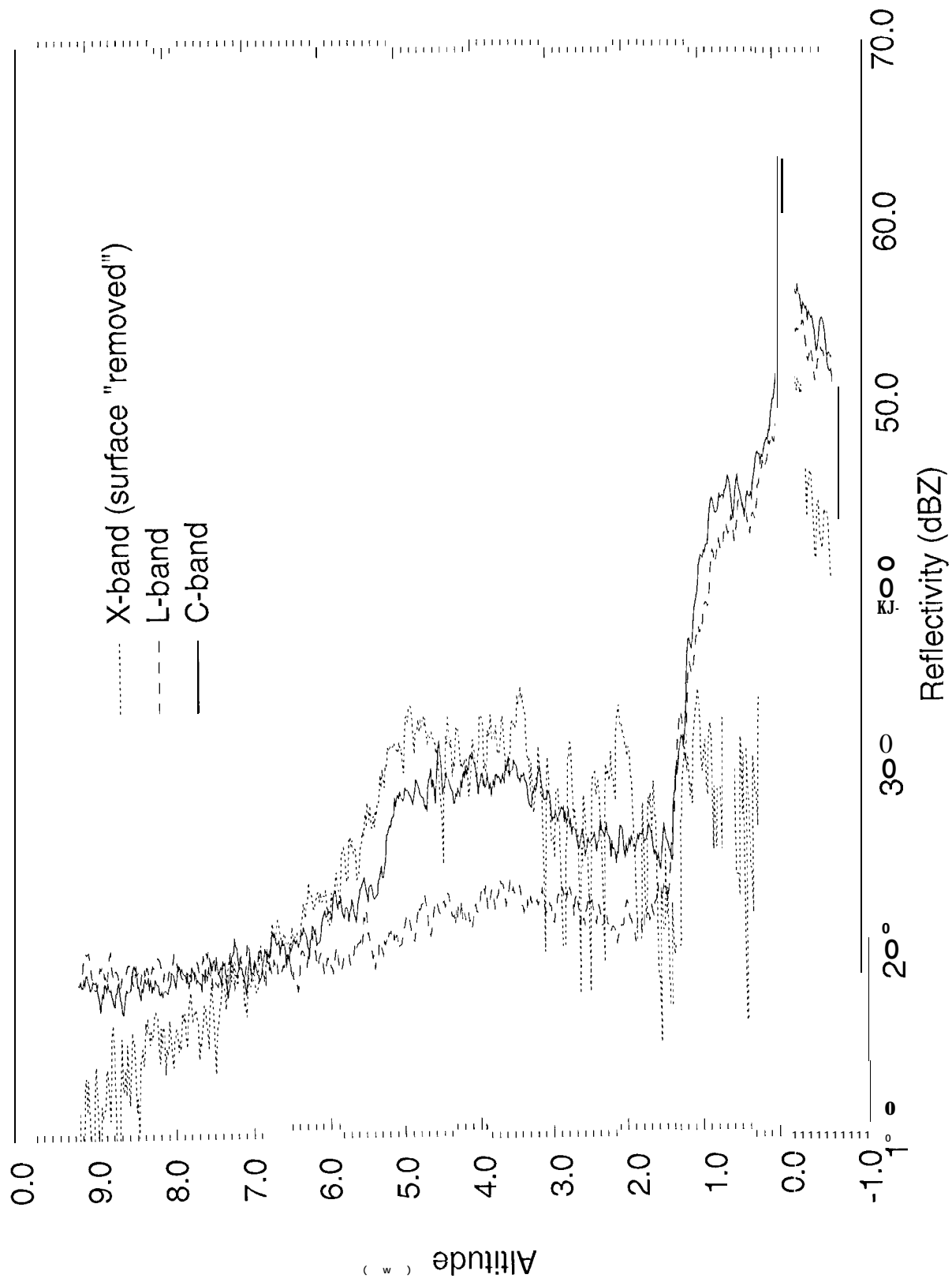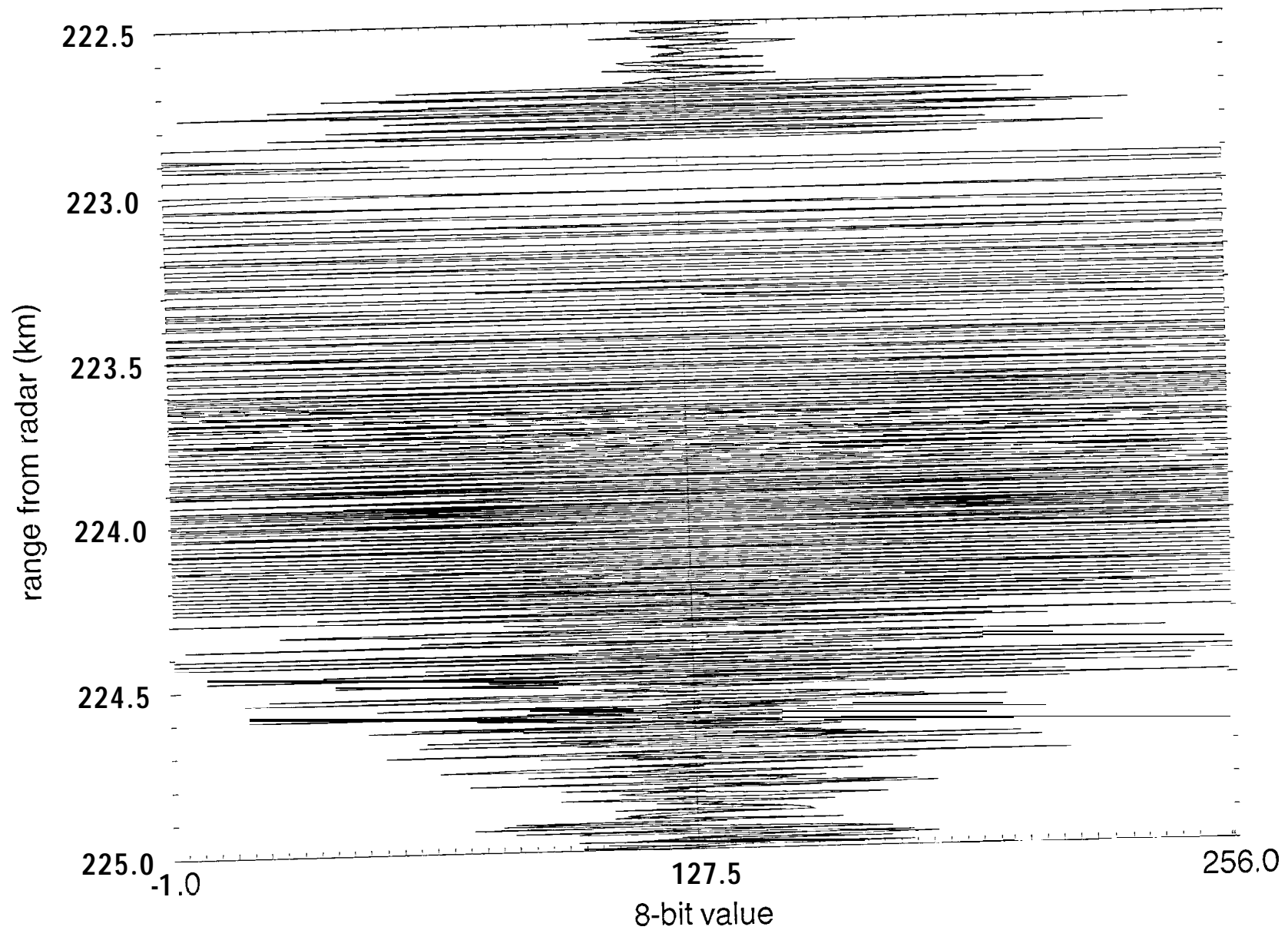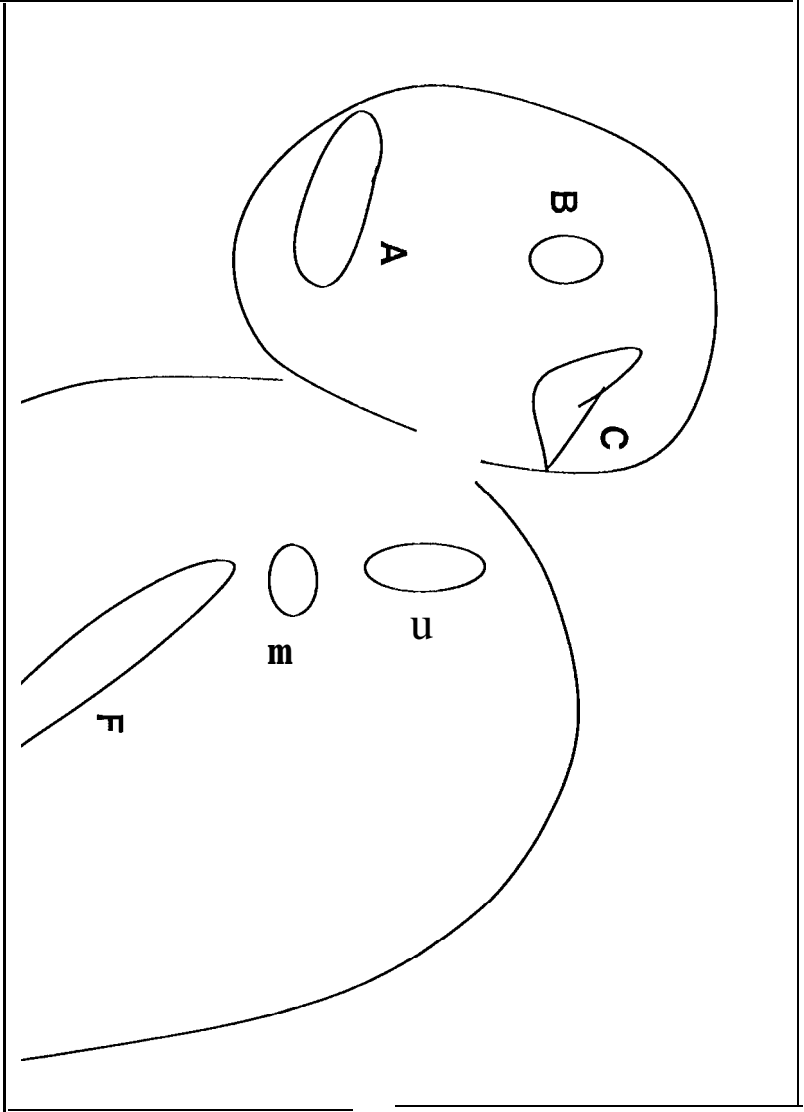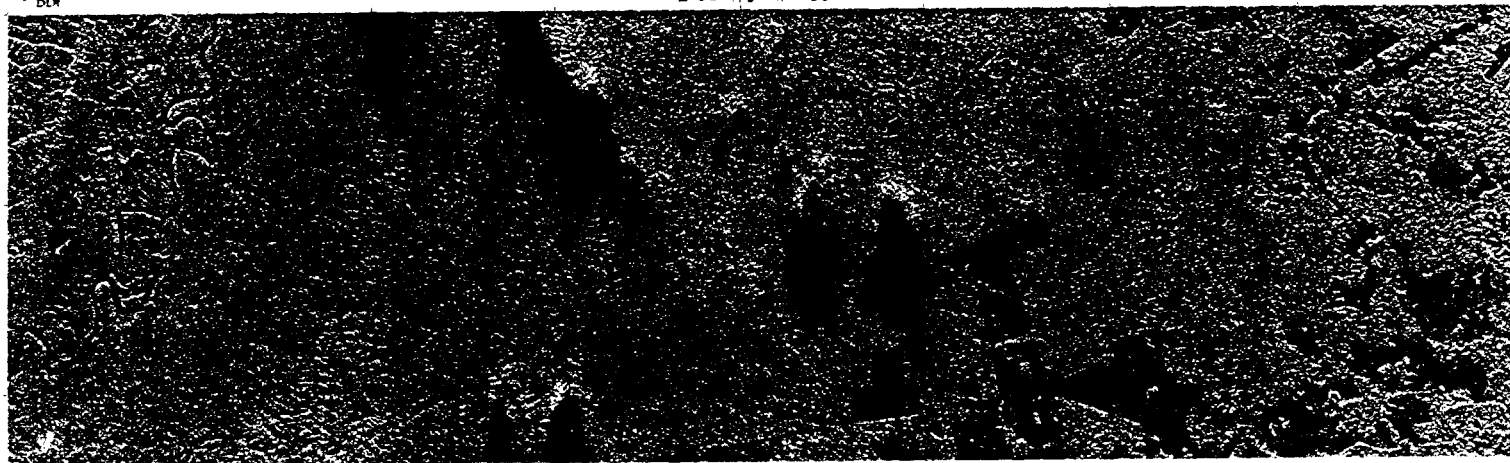
SIRC/XSAR NADIR

LDR

NASA/J PL ARMAR NADIR

LDR

NCAR/CP-2 ZENITH

LDR

Convective 1

X-band (surface "removed")
L-band
C-band

Reflectivity (dBZ)

Altitude (m)

Quantized Raw Echo

range from radar (km)

222.5

223.0

223.5

224.0

224.5

225.0

-1.0

127.5

256.0

8-bit value

,,

Mission and Sensor Parameters

Mission / Sensor	: SRL-1 / X-SAR
Data Take ID	: 103.06
Radar Frequency / Polarisation	: 9.6 GHz / VV
Accompanying SIR-C Mode	: 11
Range Pulse Bandwidth	: 9.5 MHz
PRF	: 1736 Hz
Raw Data Quantization	: 6I/6Q
Orbit Direction	: descending
Antenna Direction	: right looking
Track Angle at Image Center	: 149.9°
Incidence Angle at Image Center	: 48.6°

Archiving Parameters

D-PAF Job Number	: Order109539
Product Generation	: DMS controlled

D-PAF Product Identification
X1SAR94041518455GMGD___DP19940630172746

Image and Processing Parameters

Site Name	: Sena Madureira / Brazil
Lat/Long at Image Center	: S 9°-21' / W 58°-12'
GMT at Image Center	: 15-APR-1994/18:45:56.191
MET at Image Center	: 006:07:40:56.191
Processing Date	: 30-JUN-1994/17:27:46
Image Generation Date	, 1-JUL-1994 10:24
Processor S/W Version	: 02.00.00
Image Size	: 8196 lines x 2384 pixels
Pixel Spacing	: rng 12.5 m / az 12.5 m
Nominal Resolution	: rng 24.9 m / az 25.2 m
Equivalent Number of Looks	: rng 1.0 x az 3.5
Geometric Representation	: ground
Doppler Centroid at Image Center	: 1620 Hz
Raw Data S/N Ratio	: 23.8 dB
Radiometric Corrections	: absolutely calibrated

d

dr

r

s

random medium
(rain)

surface (ocean)